Antarctic Intermediate Water and Subantarctic Mode Water Formation in the Southeast Pacific: The Role of Turbulent Mixing

BERNADETTE M. SLOYAN

Centre for Australian Weather and Climate Research, CSIRO, and CSIRO Wealth from Oceans National Research Flagships, Hobart, Tasmania, Australia

LYNNE D. TALLEY AND TERESA K. CHERESKIN

Scripps Institution of Oceanography, La Jolla, California

RANA FINE

Rosenstiel School of Marine and Atmospheric Science, University of Miami, Miami, Florida

JAMES HOLTE

Scripps Institution of Oceanography, La Jolla, California

(Manuscript received 8 August 2008, in final form 26 January 2010)

ABSTRACT

During the 2005 austral winter (late August–early October) and 2006 austral summer (February–mid-March) two intensive hydrographic surveys of the southeast Pacific sector of the Southern Ocean were completed. In this study the turbulent kinetic energy dissipation rate ϵ, diapycnal diffusivity κ, and buoyancy flux J_b are estimated from the CTD/O_2 and XCTD profiles for each survey. Enhanced κ of $O(10^{-3}$ to 10^{-4} m^2 s$^{-1})$ is found near the Subantarctic Front (SAF) during both surveys. During the winter survey, enhanced κ was also observed north of the ''subduction front,'' the northern boundary of the winter deep mixed layer north of the SAF. In contrast, the summer survey found enhanced κ across the entire region north of the SAF below the shallow seasonal mixed layer. The enhanced κ below the mixed layer decays rapidly with depth. A number of ocean processes are considered that may provide the energy flux necessary to support the observed diffusivity. The observed buoyancy flux (4.0×10^{-8} m^2 s^{-3}) surrounding the SAF during the summer survey is comparable to the mean buoyancy flux (0.57×10^{-8} m^2 s^{-3}) associated with the change in the interior stratification between austral summer and autumn, determined from Argo profiles. The authors suggest that reduced ocean stratification during austral summer and autumn, by interior mixing, preconditions the water column for the rapid development of deep mixed layers and efficient Antarctic Intermediate Water and Subantarctic Mode Water formation during austral winter and early spring.

1. Introduction

The characteristic features of Subantarctic Mode Water (SAMW: pycnostad, potential vorticity minimum, and oxygen maximum) and Antarctic Intermediate Water (AAIW: salinity minimum) extend northward into the Atlantic, Indian, and Pacific subtropical gyres from the Subantarctic Front (SAF)—the northernmost front of the Antarctic Circumpolar Current (ACC) system (McCartney 1977; Hanawa and Talley 2001). SAMW and AAIW are the prominent middepth (500–1000 m) water masses in the Southern Hemisphere oceans. They supply nutrients and ventilate the subtropical thermocline and are an important component of the global heat, freshwater, and carbon budgets and the global overturning circulation.

Climate studies have observed decadal and longer period variability in the temperature and salinity of SAMW and AAIW in the subtropical thermoclines and Southern Ocean (Wong et al. 1999; Bindoff and McDougall 2000; Gille 2002; Bryden et al. 2003). The salinity variability has been linked to anthropogenic climate change (Banks and

Corresponding author address: Bernadette Sloyan, CSIRO Marine and Atmospheric Research, GPO 1538, Hobart, TAS 7001, Australia.
E-mail: bernadette.sloyan@csiro.au

DOI: 10.1175/2010JPO4114.1

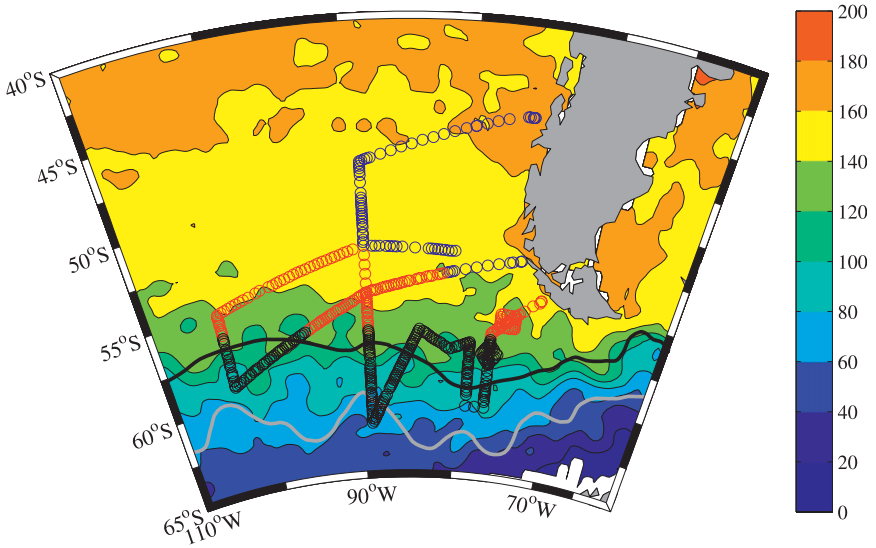

FIG. 1. Distribution of CTD and XCTD stations for the 2005 austral winter survey. A similar survey track was completed in 2006 austral summer. Hydrographic stations are grouped into three distinct dynamical regions: SAF and PF frontal (black), winter deep mixed layer (red), and subduction (blue). Also shown is Archiving, Validation, and Interpretation of Satellite Oceanographic data (AVISO) dynamic topography field (color, cm) averaged for the survey period and mean position of SAF (black) and PF (gray) from Orsi et al. (1995).

Bindoff 2003) or substantial internal ocean variability in SAMW and AAIW formation processes and rates (McDonagh et al. 2005). These studies suggest the need for a greater understanding of the processes involved in the formation of these climate-sensitive water masses so that we can fully understand the potential impact of climate change and variability on the ocean circulation and global climate.

Along the circumpolar pathway two regions have been identified as principal formation sites of SAMW: the southeast Indian (80°–130°E) and southeast Pacific (120°–70°W) sectors of the Southern Ocean (e.g., McCartney 1982; Talley 1999; Hanawa and Talley 2001; Sloyan and Rintoul 2001; Dong et al. 2008; Sallée et al. 2010). At these sites, winter mixed layer depths (MLDs) of greater than 500 m have been observed. In the southeast Pacific, SAMW and AAIW have similar salinity and temperature characteristics, and this property overlap has led to the suggestion that AAIW is the densest variety of SAMW (McCartney 1977).

Numerous processes, based on observational and modeling studies, have been postulated to influence the formation rate and properties of SAMW and AAIW (McCartney 1982; Ribbe and Tomczak 1997; Marsh et al. 2000; Sloyan and Rintoul 2001; Karsten and Marshall 2002; Rintoul and England 2002; Sallée et al. 2006). These processes include convection driven by air–sea fluxes, Ekman transport across the SAF, eddy (lateral) and turbulent (vertical) mixing across the SAF, and mixing within and at the base of the mixed layer. Although ideas abound about the mechanisms involved in the formation of SAMW and AAIW, we are only now beginning to build a climatology of the seasonal evolution of SAMW and AAIW properties via the Argo program and dedicated hydrographic process studies. Observations (and continuation of the observational programs) are vital in our endeavor to qualify and assess the relative importance of all of the processes along the circumpolar pathway involved in the formation of these water masses.

In the 2005 austral winter (August–October) and 2006 austral summer (January–March), two hydrographic surveys in the southeast Pacific sector of the Southern Ocean by the R/V *Knorr* were completed as a first step to characterize the formation processes of SAMW and AAIW and the seasonal upper-ocean restratification (Fig. 1). These surveys included the contemporaneous collection of conductivity–temperature–depth and oxygen (CTD/O_2), nutrient, shipboard acoustic Doppler current profiler (SADCP), lowered ADCP (LADCP), expendable CTD (XCTD), underway meteorological, and carbon and chlorofluorocarbon (CFC) data. All observations, except for carbon and CFC data, were collected during both surveys.

In this study, we estimate the turbulent kinetic energy dissipation rate ϵ, diapycnal diffusivity κ, and buoyancy flux J_b from the CTD/O_2 and XCTD profiles for each survey. Enhanced ϵ, κ, and J_b are found near the SAF

during both surveys: north of the SAF during the summer survey and north of the ''subduction front'' during the winter survey. The enhanced diffusivity below the mixed layer decays rapidly with depth. We consider a number of processes that may provide the energy needed to sustain the observed diffusivity. Of these, we find that the wind energy input to the ocean, associated with synoptic weather systems, provides some of the energy necessary to support the observed diffusivity. The observed buoyancy flux (4.0×10^{-8} m^2 s^{-3}) surrounding the SAF during the 2006 austral summer survey is comparable to the mean buoyancy flux (0.57×10^{-8} m^2 s^{-3}) associated with the change in the interior stratification from austral summer to autumn, determined from Argo profiles. We suggest that removal of ocean stratification during austral summer and autumn by interior mixing preconditions the water column for the rapid development of deep mixed layers and efficient AAIW and SAMW formation during austral winter and early spring.

2. Data

In this study we use the CTD, XCTD, SADCP, and underway wind speed and direction data collected during the two hydrographic surveys (Fig. 1).

a. CTD/O_2 and XCTD

1) CTD/O_2

CTD/O_2 stations (135 during the winter survey and 105 during summer survey) at a nominal spacing of 55 km were collected along the survey track. The CTD/O_2 unit comprises a Sea-Bird Electronics (SBE) 9plus CTD with dual pumps and a SBE43 dissolved oxygen sensor. Laboratory calibration of the CTD conductivity, temperature, pressure, dissolved oxygen sensors, and digital reversing thermometer were performed prior to the 2005 austral winter survey. Routine CTD maintenance included soaking the conductivity and dissolved oxygen sensors in freshwater between casts to maintain sensor stability. CTD/O_2 survey data were processed and quality controlled, and salinity and oxygen sensors were calibrated against bottle salinity and oxygen data by the Oceanographic Data Facility (ODF) from Scripps Institution of Oceanography (SIO). Finally, 1-dbar bin-averaged temperature, salinity, and oxygen data were produced.

2) XCTD

During the 2005 austral winter and 2006 austral summer surveys, dense underway profiling of the upper-ocean temperature and salinity was carried out with XCTDs. The XCTDs were digital Tsurumi-Seiki Co. (TSK) probes purchased from Sippican, Inc. and manufactured by TSK. The XCTDs were deployed by a hand launcher from the stern of the vessel. The sampling spacing (8–15 km) supplemented the full-depth CTD stations.

Ship-supplied equipment (computer, deck unit, and launcher) were used to acquire the XCTD data during austral winter. The deck unit was the Sippican MK-21 model. The Sippican data acquisition software versions used were WinMK21 v2.1.2, MK21COEF v2.3.1, and MK21AL v2.5.1. During the 2005 austral winter survey, initial failure rates of the XCTD profiles were significant. The probe failures were due to an intermittent grounding problem between the computer chassis and deck unit. Given the problems that the XCTD program experienced during the 2005 austral winter survey, SIO supplied the primary data acquisition equipment for the 2006 austral summer survey. The Sippican data acquisition software version WinMK21 SURFACE was used during the 2006 austral summer survey.

A total of 755 (406 in austral winter and 349 in austral summer) XCTD profiles were processed with the Sippican automated software when the data were first acquired. Further extensive quality control of the profile data was undertaken prior to their use in this study. XCTD temperature and salinity profiles were flagged as bad, questionable, or good as follows: 1) extreme outliers in the XCTD temperature and salinity profile data were flagged bad through comparison with seasonal profiles from the CSIRO Atlas of Regional Seas (CARS2006a; available online at http://www.marine.csiro.au/~dunn/cars2006/index.html) in a 2° radius of the XCTD profile. CARS2006a is a 0.5° × 0.5° gridded climatology of seasonal ocean water properties. CARS2006a includes Argo temperature and salinity profile data. Argo dominates the available data in the southeast Pacific sector of the Southern Ocean, resulting in a median climatology age of 2002 and improved representation of the seasonal cycle in the survey region from climatologies that only use CTD profiles. 2) XCTD salinity and temperature profiles were compared to surrounding survey CTD profiles. Dubious XCTD temperature and salinity profiles were given bad data quality flags. Only XCTDs for which both temperature and salinity profiles were flagged good and that reached a depth greater than 500 m were used in this study. These quality control procedures resulted in the use of 641 XCTD profiles (312 for 2005 austral winter and 329 for 2006 austral summer). Examination of the XCTD temperature and salinity profiles shows high-frequency noise in the salinity data. Similar to Thompson et al. (2007), a 3-m filter was applied to the XCTD salinity and temperature profiles to remove the high-frequency noise.

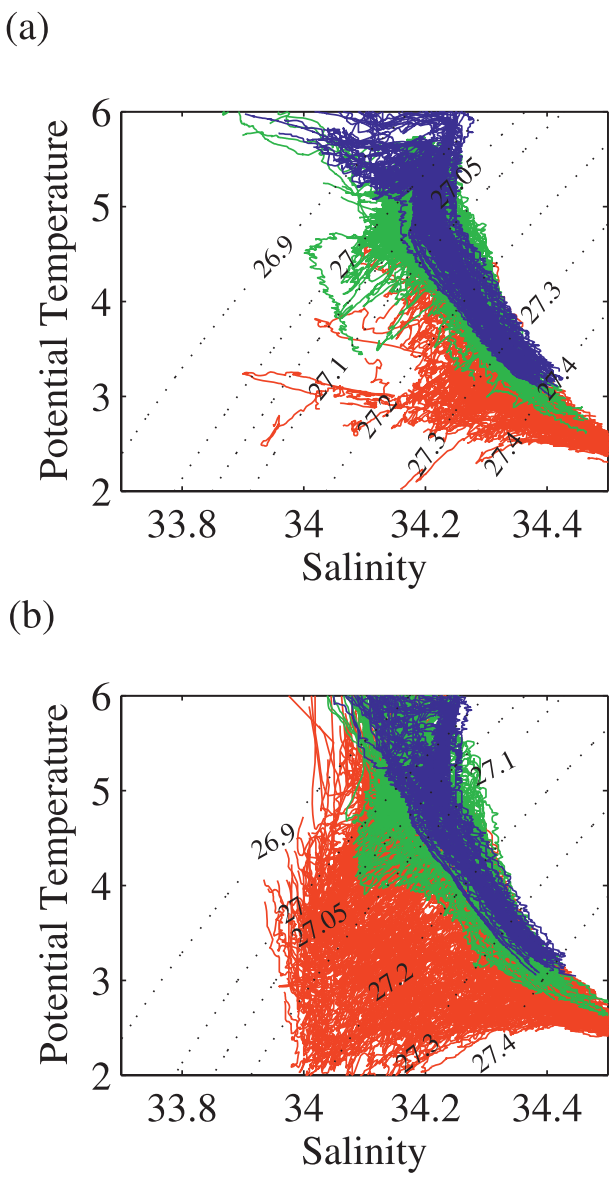

FIG. 2. Potential temperature (°C)–salinity diagram for all profile data in the (a) 2005 austral winter survey and (b) 2006 austral summer survey. Profiles near or south of the SAF (red), in the winter deep mixed layer region (green), and in the subduction region (blue) are identified. Contours of potential density (dotted black) are also shown. Contours are 26.9, 27.0, 27.05, 27.4, 27.2, 27.3, and 27.4 kg m^{-3}.

3) COMBINED PROFILE DATA

The XCTD profiles and CTD station data were combined, resulting in a total of 447 and 434 profiles for the 2005 austral winter and 2006 austral summer surveys, respectively (Fig. 2). XCTD profiles include 70% and 76% of the 2005 austral winter and 2006 austral summer profiles used in this study, respectively. The mixed layer depth (MLD) for each profile is determined here using a threshold method as a density change of $\Delta\rho = 0.03$ kg m^{-3} from 10 m (de Boyer Montégut et al. 2004; Holte and Talley 2009). The vertical temperature and salinity distributions along 89°W of the combined XCTD and CTD data for the 2005 austral winter and 2006 austral summer are shown in Fig. 3. For the 2005 austral winter survey the SAF (~59°S) is identified by the large horizontal density gradient that extends from the sea surface to 1100 m. In austral winter, the mixed layer rapidly deepens on the northern side of the SAF; this region of deep mixed layers extends to 53°S (Fig. 3). In the 2006 austral summer, a warm and fresh surface layer results in a strong seasonal pycnocline, and nearly constant MLDs of ~60 m are found along 89°W (Fig. 3).

b. *SADCP*

The 5-min-averaged SADCP data used in this study were collected by an RD Instruments 75-kHz Ocean Surveyor (OS75) mounted in the hull of the R/V *Knorr*. The OS75 worked continuously during both cruises, and the main problems with data quality were bubble sweepdown when the bow thruster was used to maintain station and during rough weather and heavy seas. In this study we use only the underway data.

The OS75 operating parameters were 70 depth bins and a 16-m blank, range bin, and pulse length. Single ping ADCP data and ancillary navigation streams (position and heading) were collected at sea and then later processed and edited using software (UHDAS and CODAS3) written by E. Firing and J. Hummon, University of Hawaii. The primary heading source was the ships gyrocompass and heading corrections were made using the R/V *Knorr* Position and Orientation System (POS MV). Accurate position and heading data from the ship's navigation system provide absolute currents with an estimated error of 1–2 cm s^{-1} (Chereskin and Harris 1997). The shallowest velocity measurement was 37 m, with a vertical sampling at 16-m intervals to approximately 1000 m.

c. *Wind data*

On both surveys, an Improved Meteorological (IMET) suite of sensors was installed on the R/V *Knorr* meteorological mast. The suite of sensors included wind speed and direction sensors. The instruments on the IMET package were calibrated prior to the 2005 austral winter survey. The meteorological data (30-s interval) were collected using the SIO Shipboard Technical Support (STS) Meteorological Acquisition (METAcq) system. True wind speed was computed following Smith et al. (1999). A 5-min-averaged wind speed and direction time series, coincident with the SADCP time series, was used in this study.

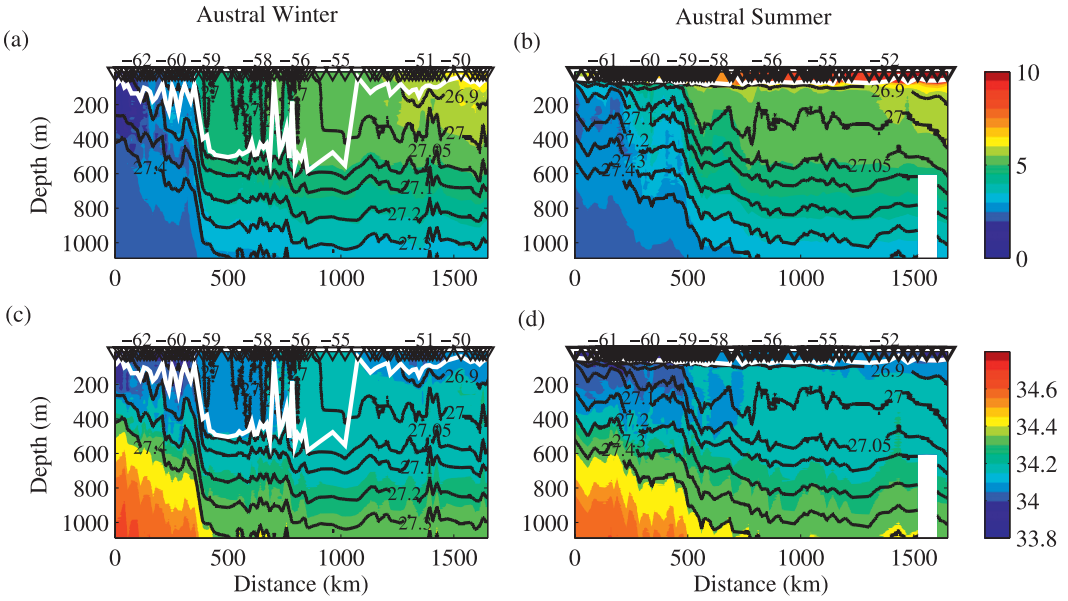

FIG. 3. Property distribution along 89°W for the (left) 2005 austral winter and (right) 2006 austral summer surveys of (top) potential temperature (°C) and (bottom) salinity. Also shown are potential density (σ_θ, kg m^{-3}) distribution (black) and mixed layer depth (white). Potential density contours (black) are 26.9, 27.0, 27.05, 27.1, and 27.3 kg m^{-3}, where SAMW is defined within $26.6 \le \sigma_\theta \le 27.05$ kg m^{-3} and AAIW is within $27.05 \le \sigma_\theta \le 27.4$ kg m^{-3}. Profile positions are shown on the upper x axis, and the latitude of approximately every seventh profile is given.

The IMET wind data were compared to the 6-hourly blended satellite derived wind data provided by the European Space Agency Processing and Archiving Facility (CERSAT) as a consistency check of the ship observations (blended wind data were obtained online at ftp://ftp.ifremer.fr/ifremer/cersat/products/gridded/mwf-blended/data/6-hourly). The IMET wind data (wind speed and direction) and wind stress for the two survey periods are in good agreement with 6-hourly blended satellite derived wind data (not shown).

3. Turbulent kinetic energy estimates from density profiles

a. Background

Turbulence in the ocean is spatially patchy, with typical length scales given by the Ozmidov scale L_o, which is related to the turbulent kinetic energy dissipation rate ϵ and the buoyancy frequency N (Thorpe 1977). For a turbulent patch, the Ozmidov scale is

$$L_o = \left(\frac{\epsilon}{N^3}\right)^{1/2}, \tag{1}$$

where L_o is the distance a parcel would move if all of the kinetic energy was transferred to potential energy and, therefore, a measure of the maximum overturning length scale associated with mixing (Ferron et al. 1998).

Measuring the turbulent kinetic energy dissipation rate directly is difficult. Thorpe (1977) showed that the Ozmidov scale can be related to the length scale of density inversions that arise from ocean turbulence; these can be estimated from available density profile data. The Thorpe scale L_T is the root-mean-square of the vertical displacement (d') of a water parcel in a gravitationally unstable region when the profile is reordered to be continuously gravitationally stable; that is, $L_T = \sqrt{\langle d'^2 \rangle}$, where the angle brackets denote an averaging process. Microstructure studies that directly measure the Ozmidov scale L_o have been used to define a relationship between L_o and L_T:

$$L_o = aL_T, \tag{2}$$

where a varies between 0.65 and 0.98 (Dillon 1982; Crawford 1986; Ferron et al. 1998). Here we use $a = 0.8$, as suggested by Dillon (1982).

From (1) and (2) we can estimate ϵ using L_T determined from gravitationally unstable regions within a given density profile as

$$\epsilon = a^2 L_T^2 \langle N \rangle^3, \tag{3}$$

where the buoyancy frequency N is given by $N^2 = -g(d\rho/dz)/\rho$. Here, $\langle N \rangle$ is the averaged buoyancy frequency over the reordered unstable region, which is typically 10 m.

Following Osborn (1980), it is common to relate ϵ to diapycnal eddy diffusivity κ as

$$\kappa = \Gamma\langle\epsilon\rangle N^{-2}, \quad (4)$$

where N is the background buoyancy frequency, calculated here with a smoothing scale of 100 m, as (4) relates to the turbulent diffusivity working on the background density gradient (Ferron et al. 1998); $\langle\epsilon\rangle$ is the mean turbulent kinetic energy dissipation rate over the thickness of a water mass layer; and Γ is the mixing efficiency ($\Gamma = 0.2$) (Thorpe 2005).

Mixing events result in the vertical exchange of buoyancy by the dissipation of turbulent kinetic energy (Osborn 1980; St. Laurent et al. 2001). We can then define the water mass layer buoyancy flux associated with mixing events by

$$-J_b = \Gamma\langle\epsilon\rangle, \quad (5)$$

where the turbulent kinetic energy dissipation rate $\langle\epsilon\rangle$ is estimated from (3). In this study, we focus on the diffusivity (4) and buoyancy flux (5) associated with interior mixing in the SAMW and AAIW density layers.

b. Method

CTD and XCTD density profiles were reordered to be gravitationally stable. Following Ferron et al. (1998), Thorpe scale L_T was determined for unstable patches in a density profile. Overturns were determined for a density difference of $2\delta\rho$, where $\delta\rho = 1 \times 10^{-3}$ kg m^{-3} (Thompson et al. 2007). Figure 4 shows temperature, salinity, and potential density XCTD profiles and L_T due to density inversions in the subduction region of the 2005 austral winter and 2006 austral summer surveys; L_T of length 10–15 m are typically found below the mixed layer and near the SAF in both surveys.

Potentially spurious overturns were eliminated by applying the Galbraith and Kelley (1996) minimum thickness test. They suggest that a resolvable overturn in a given density profile must be greater than

$$L_{\rho_{\min}} = 2\frac{g\ \delta\rho}{N^2\rho_0},$$

where ρ_0 is the mean density of the water column. In this study, the application of the Ferron et al. (1998) procedure to detect overturns ensures that any overturn must have a density difference of greater than $2\delta\rho$, and the application of the $L_{\rho_{\min}}$ applies a stratification criteria to the minimum length of a detectable overturn in regions of weak stratification. Finally, a minimum overturn length of 3 m was applied based on the smoothing applied to XCTD profiles. Quality control procedures applied to CTD and XCTD data removed the need to apply the water mass criterion (Galbraith and Kelley 1996).

We calculate the L_T and ϵ, below the mixed layer, for each overturn patch in a given density profile. We exclude the mixed layer since (4) is not valid in regions where mixing is dominated by convective processes (Johnson and Garrett 2004). Then N^2 is estimated, over 10 m for (3) and 100 m for (4), as the slope of a linear fit to the specific volume anomaly depth profiles using the adiabatic leveling method (Bray and Fofonoff 1981). SAMW and AAIW water masses are divided into six layers defined by potential density surfaces σ_θ = 26.9, 27.0, 27.05, 27.1, 27.2, 27.3, and 27.4 kg m^{-3}. SAMW is defined within $26.9 \le \sigma_\theta \le 27.05$ kg m^{-3}, and AAIW is defined within $27.05 \le \sigma_\theta \le 27.4$ kg m^{-3}. Water mass layer mean κ and $-J_b$ from (4) and (5), respectively, are determined for each profile of the austral winter and summer surveys.

4. Diffusivity and buoyancy flux estimates

The austral winter and summer surveys were designed to sample the large geographical and diverse dynamical region of the southeast Pacific sector of the Southern Ocean including the frontal region of the SAF and Polar Front (PF), the deep mixed layer region where AAIW and SAMW formation occurs, and the subduction region (Figs. 1,2). On each survey the SAF was crossed six times and the PF twice. During the 2005 austral winter survey the region of deep mixed layers extended in a southeast direction north of the SAF from 50°S, 103°W to 55°S, 70°W. North of the deep mixed layer region, a distinct change in surface salinity and decrease in the depth of the mixed layer marked the northern boundary of the active convection region (Fig. 3). These features denote the subduction front, and profiles north of this boundary indicate that SAMW is subducted into the subtropical Pacific gyre.

Water mass layer mean κ along 89°W shows areas of enhanced diffusivity on most profiles (Fig. 5). In the 2005 austral winter survey patches of enhanced diffusivity are found in the frontal region surrounding the PF and SAF within $27.1 \le \sigma_\theta \le 27.3$ kg m^{-3} (Fig. 5). Beneath the winter deep mixed layers, north of the SAF (Fig. 3), only isolated patches of enhanced diffusivity are found (Fig. 5). In the subduction region, equatorward of the deep mixed layer region, enhanced diffusivity is found in SAMW layers ($26.9 \le \sigma_\theta \le 27.05$ kg m^{-3}) and the upper AAIW layer ($27.05 \le \sigma_\theta \le 27.1$ kg m^{-3}); κ decreases in the densest AAIW layers ($27.1 \le \sigma_\theta \le 27.4$ kg m^{-3}). The 2006 austral summer survey along 89°W shows a similar pattern and magnitude of enhanced

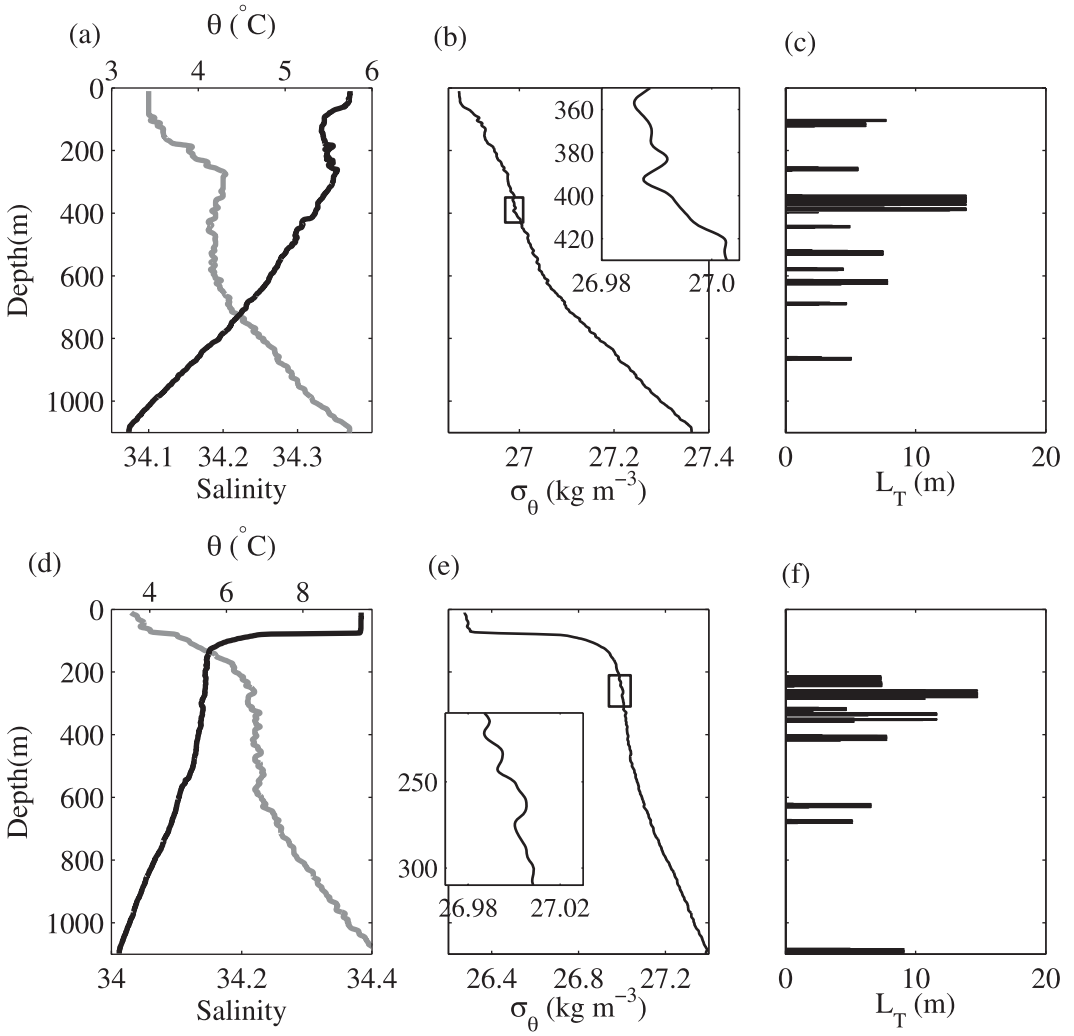

FIG. 4. Typical property profiles in the subduction region for the (top) 2005 austral winter and (bottom) 2006 austral summer surveys: (a),(d) potential temperature (black) and salinity (gray) profiles; (b),(e) potential density; and (c),(f) Thorpe scale L_T. Insets in (b) and (e) show one unstable region in the density profile.

diffusivity, except that enhanced diffusivity is found across the entire region north of the SAF (Fig. 5).

The 2005 austral winter and 2006 austral summer profiles of diffusivity and buoyancy flux for SAMW and AAIW layers in each region (Fig. 1) are averaged to show spatial differences in the diffusivity and buoyancy flux (Fig. 6). In both surveys the magnitudes of the diffusivity and buoyancy fluxes are largest in the upper water column (SAMW and upper AAIW layers) and decay with increasing density (Fig. 6) (Excluding CTD profiles did not result in a qualitative difference in regional estimates of water mass layer mean κ or J_b from those shown. Therefore, both XCTD and CTD profiles are used in this study). In austral winter the largest diffusivities and buoyancy fluxes are found in the SAMW layers in the subduction region (Figs. 6a,c). During austral winter the SAMW layers immediately north of the SAF are mostly within the mixed layer and are not included in the diffusivity calculations. This explains the significant diffusivity and buoyancy flux decrease between the subduction and deep mixed layer regions for SAMW layers. In austral summer, enhanced diffusivity and buoyancy fluxes are found across the entire region north of the SAF (Figs. 6b,d). In the frontal region (SAF/PF), diffusivity and buoyancy fluxes in the AAIW layers are slightly larger in austral winter than in austral summer (Fig. 6).

The enhanced diffusivities $O(10^{-3}\ \mathrm{m^2\ s^{-1}})$ directly beneath the mixed layer and decaying to $O(<10^{-4}\ \mathrm{m^2\ s^{-1}})$ by 1000 m are similar to estimates by Cisewski et al. (2005) and Thompson et al. (2007). This study shows that the enhanced diffusivity has an associated buoyancy flux $O(10^{-8}$ to $10^{-9}\ \mathrm{m^2\ s^{-3}})$. The enhanced upper-ocean

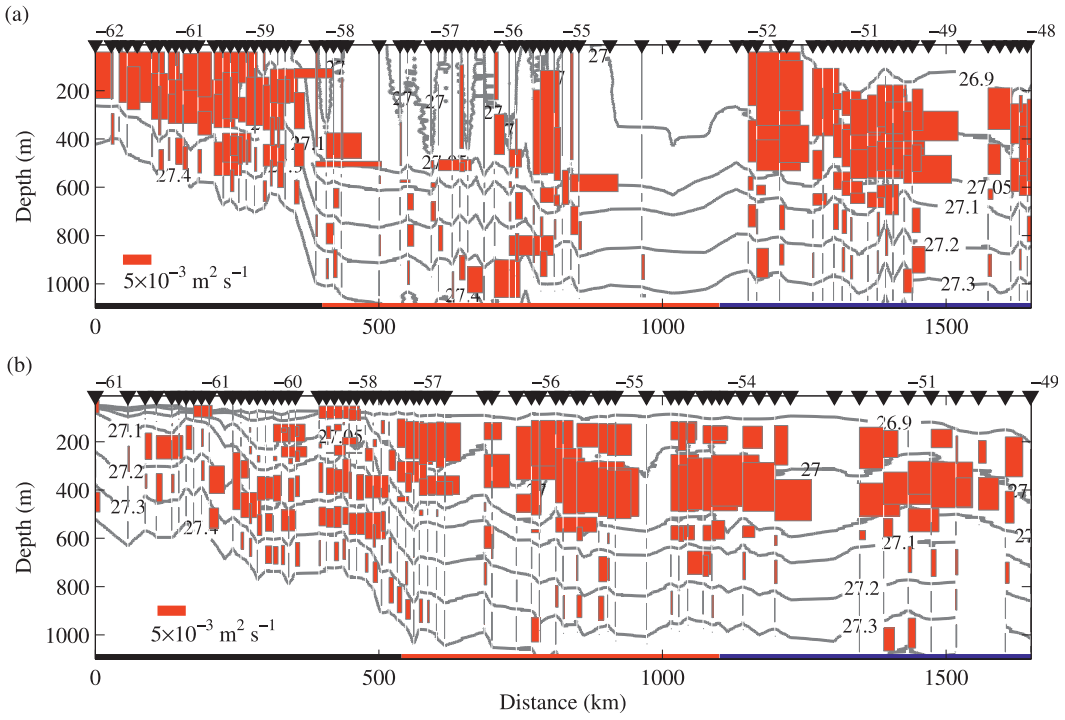

FIG. 5. Water mass layer mean diffusivity along 89°W for the (a) 2005 austral winter and (b) 2006 austral summer surveys. The horizontal bar is equal to the magnitude of the water mass layer mean diffusivity. Profile diffusivity is shown between density surfaces (gray contours) that define the water mass layers of SAMW ($26.9 \leq \sigma_\theta \leq 27.05$ kg m^{-3}) and AAIW ($27.05 \leq \sigma_\theta \leq 27.4$ kg m^{-3}). Contours are 26.9, 27.0, 27.05, 27.4, 27.2, 27.3, and 27.4 kg m^{-3}. Profile positions are shown on the upper x axis, and the latitude of approximately every eighth profile is given. The latitudinal extent of the three different regions based on water mass properties and ocean dynamics are shown on the lower x axis: 1) near or south of the SAF (black); 2) winter deep mixed layer region (red); and 3) the SAMW and AAIW subduction region (blue).

diffusivity and buoyancy flux found in the southeast Pacific sector of the Southern Ocean are one to two orders of magnitude larger than those observed in other open ocean thermocline regions (Ledwell et al. 1993).

We note that Thompson et al. (2007) find a seasonal diffusivity signal with larger diffusivity in winter in the upper water column (100–400 m), whereas between 400 and 1000 m, summer diffusivity is similar to or slightly larger than winter diffusivity. In contrast, we find large diffusivity and buoyancy fluxes north of the SAF in summer (Fig. 6b, $26.9 \leq \sigma_\theta \leq 27.0$ kg m^{-3}) when the mixed layer is shallow. It is likely that our results differ from Thompson et al. because their upper layer was actually well beneath the shallow summer mixed layer (<60 m, Fig. 3) and, therefore, did not include the enhanced diffusivity immediately beneath the summer shallow mixed layer.

5. Potential drivers of the observed ϵ

The observed ϵ could be sustained by a number of different ocean processes or forcing mechanisms, including double diffusion, wind forcing, mesoscale eddies, and remotely forced internal waves that propagate into the region. In this section, we consider some of these processes to determine the possible mechanisms that drive the observed diffusivity.

a. Double diffusion

We first look at the extent to which the observed κ could be the result of double diffusive convection owing to either salt fingering or double diffusive layering. The density ratio,

$$R_\rho \equiv \alpha \frac{\partial \theta}{\partial z} \Big/ \beta \frac{\partial \mathrm{S}}{\partial z},$$

provides an indication of the presence and strength of double diffusion, where the thermal expansion is $\alpha = -\rho^{-1}\partial\rho/\partial\theta$ and the haline contraction is $\beta = \rho^{-1}\partial\rho/\partial\mathrm{S}$; $\partial\rho/\partial\theta$ and $\partial\rho/\partial\mathrm{S}$ were calculated using the Equation of State software library (Jackett et al. 2006). Following Ruddick (1983) and McDougall et al. (1988), to remove the ambiguity of the sign of the exponent in the definition of R_ρ, we determine the Turner angle Tu, defined as the four-quadrant ($[-\pi, \pi]$) arctangent

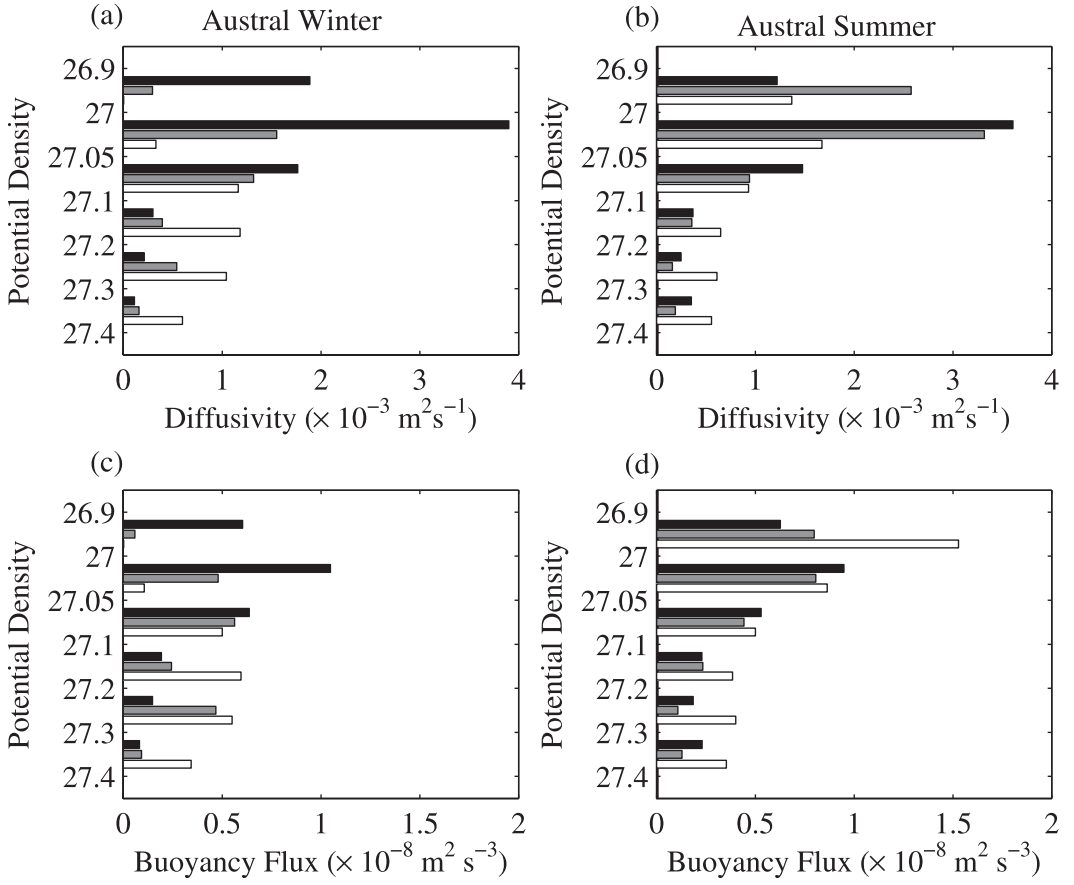

FIG. 6. Water mass layer mean (a),(b) diffusivity and (c),(d) buoyancy flux for the 2005 austral winter and 2006 austral summer surveys. Survey profiles are divided into three different regions based on water mass properties and ocean dynamics (Fig. 1): 1) near or south of SAF (white bar), 2) winter deep mixed layer region (gray bar), and 3) SAMW and AAIW subduction region (black bar). The boundary between the winter deep mixed layer and subduction regions for the 2006 austral summer survey is taken from the 2005 austral winter survey.

$$\mathrm{Tu} = \tan^{-1}\left(\alpha\frac{\partial\theta}{\partial z} - \beta\frac{\partial \mathrm{S}}{\partial z}, \alpha\frac{\partial\theta}{\partial z} + \beta\frac{\partial \mathrm{S}}{\partial z}\right), \qquad (6)$$

where Tu is given in degrees of rotation and $R_\rho = -\tan(\mathrm{Tu} + 45°)$. Salt fingering occurs for the range $45° < \mathrm{Tu} < 90°$, with strongest salt fingering for $75° < \mathrm{Tu} < 90°$ corresponding to $1 < R_\rho < 2$. Double diffusive layering occurs for the range $-90° < \mathrm{Tu} < -45°$, with strongest double diffusive mixing for $-90° < \mathrm{Tu} < -75°$, corresponding to $1 < R_\rho < 0.5$. Between $-45°$ ($R_\rho = 0$) and $45°$ ($R_\rho \pm \infty$) Tu represent regions where the stratification is stably stratified and $|\mathrm{Tu}| > 90°$ are statically unstable portions of the water column.

The Turner angle Tu was calculated and its water mass layer mean determined (Fig. 7). More than 80% of water mass layer mean Tu are stably stratified in both surveys for the three regions: near or south of the SAF, in the winter deep mixed layer region, and in the subduction region (Fig. 7). Weak salt fingering of approximately 10% is found in the subduction region in both austral winter and summer surveys. Fewer than 5% of the profiles indicate weak salt fingering in the winter deep mixed layer region and near the SAF. Along-track Tu for the 2005 austral winter and 2006 austral summer surveys shows that weak salt fingering ($45° < \mathrm{Tu} < 75°$) is found at the northern boundary of the survey region and during the summer survey near the SAF/PF in the SAMW layers (Fig. 8). AAIW is stably stratified for both surveys (Fig. 8). This suggests that weak salt fingering could be a source of enhanced κ in SAMW in the frontal region during the 2006 austral summer survey.

b. Wind

1) NET WIND ENERGY FLUX

Over the Southern Ocean two dominant atmospheric patterns exist. The subtropical ridge is found at ~ 29°S in austral winter and 37°S in austral summer. The Antarctic

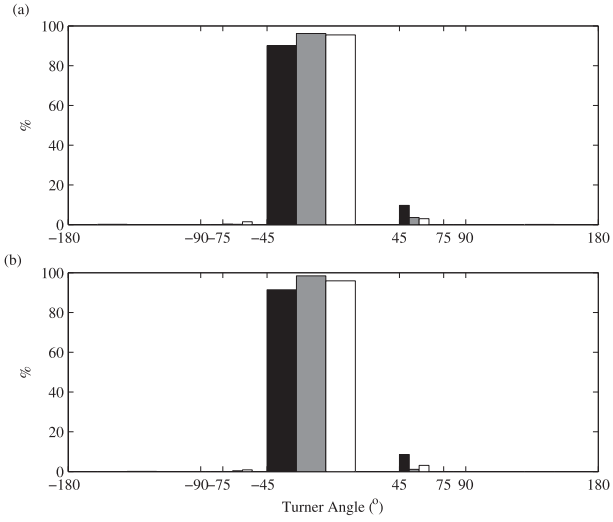

FIG. 7. Histogram of profile-averaged Tu (°) for the (a) 2005 austral winter and (b) 2006 austral summer. Survey profiles are divided into three different regions based on water mass properties and ocean dynamics: 1) near or south of SAF (white bar), 2) winter deep mixed layer region (gray bar), and 3) SAMW and AAIW subduction region (black bar). The boundary between the winter deep mixed layer and subduction regions for the 2006 austral summer survey is taken from the 2005 austral winter survey. Histogram Tu bin width is [−180°, −90°, −75°, −45°, 45°, 75°, 90°, 180°].

trough, a zone of minimum atmospheric pressure, is centered at ~65°S, but there is a significant seasonal meridional shift in the position of the trough. During March–June and September–December the trough moves northward and weakens; however, during June–September and December–March the trough moves southward and intensifies (van Loon and Shea 1988). The 2005 austral winter and 2006 austral summer surveys lie between the subtropical ridge and Antarctic trough in a zone of strong westerly winds.

The wind energy flux into the ocean is given by $\Pi_W = \tau\mathbf{u}$, where τ is the wind stress and $\mathbf{u}$ is the surface velocity (Wunsch 1998). The net wind work is given as $P_w = \int \Pi_w \, dt$, where the averaging time is 300 s. In this study, we use the 5-min-averaged underway IMET wind and SADCP mixed layer velocity time series data to estimate the wind energy flux and wind work to the ocean during the austral winter and summer surveys (Fig. 9). Synoptic weather systems with similar wind intensity occurred during both austral winter and summer surveys (Figs. 9a,b). Yuan (2004) shows that there is a higher occurrence of high wind speed (>15 m s^{-1}) events in austral winter and spring than in austral summer and autumn in the Southern Ocean but that the mean wind speed for the high wind events is similar in each season. Surface velocity south of 50°S greater than 20 cm s^{-1} identifies the SAF in both surveys (Figs. 9c,d). Efficient energy transfer from the wind field to the underlying ocean occurs when the wind and ocean currents are aligned.

The magnitude of the zonal and meridional wind stress and surface current are similar in both austral winter and summer surveys (Figs. 10a–d). Strong wind stress at the ocean surface is associated with the passage of synoptic weather systems over the survey region. The wind stress variance is similar in both the austral winter and summer survey [$\sigma_\tau = 0.01(\text{N m}^{-2})^2$]. The net wind energy flux to the ocean during both survey periods is $O(2)$ larger than the long-term mean wind energy flux (Wunsch 1998). The largest net wind energy fluxes to the ocean during both survey periods are associated with strong wind stresses that persist for 1–2 days (Figs. 10e,f). The net wind energy fluxes to the ocean during these periods result in large jumps in the cumulative wind work (Figs. 10g,h).

The wind energy flux to the surface ocean is dissipated either in the mixed layer, near the base of the mixed layer, or in the ocean interior. Transfer of wind energy to the interior ocean is suggested to be driven by the generation of wind-driven inertial currents in the mixed layer (D'Asaro 1985). Inertial currents in the mixed layer can excite near-inertial internal waves at the base of the mixed layer that propagate into the ocean interior. Near-inertial internal waves generated at the mixed layer–interior ocean boundary may dissipate energy locally or at long distances far from the generation region (Alford 2001; Plueddemann and Farrar 2006). The resultant interior mixing, by breaking near-inertial internal waves, is believed to help maintain the ocean interior stratification and may therefore be an important driver of the ocean circulation.

2) NEAR-INERTIAL WIND ENERGY FLUX

During both the 2005 austral winter and 2006 austral summer surveys the passage of synoptic weather systems resulted in an increased wind energy flux to the ocean. The synoptic weather events generate inertial motion in the mixed layer and can excite near-inertial internal waves at the mixed layer–stratified ocean boundary (D'Asaro 1985; Shcherbina et al. 2003; Plueddemann and Farrar 2006).

Following D'Asaro (1985), Alford (2001), and Plueddemann and Farrar (2006), the near-inertial energy flux generated by the wind is given by $\Pi_{W_I} = \tau\mathbf{u}_I$, where τ is the wind stress and $\mathbf{u}_I$ is the near-inertial velocity of the mixed layer. The integrated near-inertial wind energy flux, $P_{W_I} = \int \Pi_{W_I} \, dt$, is the near-inertial wind work. In this study, we have 5-min-averaged observations of wind and surface current following the survey track. Unfortunately, no moored time series data

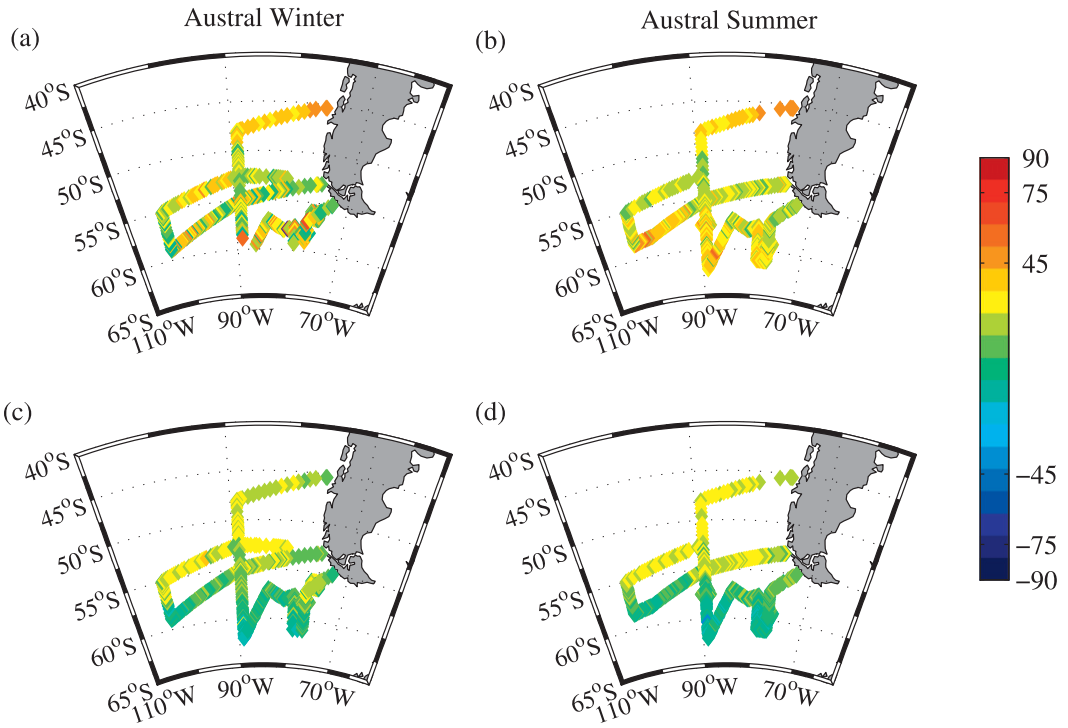

FIG. 8. The 2005 austral winter and 2006 austral summer distribution of Tu (°) for (a),(b) SAMW ($26.9 \le \sigma_\theta \le 27.05$ kg m^{-3}) and (c),(d) AAIW ($27.05 \le \sigma_\theta \le 27.4$ kg m^{-3}).

of upper-ocean currents are available from which to determine the inertial motions. However, we approximate the upper-ocean inertial current response by applying a running 4 day (96 h) bandpass filter to the along-track velocity time series data. The bandpass filter width applied is between $0.97f$ and $1.02f$, where f is the local Coriolis frequency along the survey track.

The largest inertial current response is generally associated with variability in the wind stress (Fig. 11). The near-inertial wind work is less than half of the net wind work for the 2005 austral winter and 2006 austral summer surveys (Figs. 10 and 11). For each survey period, we also calculated the wind energy flux as $\Pi_{W'} = \tau'\mathbf{u}'$, where the primed fluctuations are taken relative to survey mean wind stress and upper-ocean current (not shown). The wind energy flux and wind work calculated from the fluctuating wind stress and upper-ocean current are similar to the net wind energy flux and cumulative wind work for the 2006 austral summer survey and slightly reduced for the 2005 austral winter survey.

D'Asaro (1985) and Plueddemann and Farrar (2006) both find stronger inertial motions when the mixed layer is shallow. Stronger inertial motions with decreasing mixed layer thickness may result in a larger near-inertial wind energy flux to the ocean interior and a seasonal enhancement of diffusivity below the mixed layer (D'Asaro 1985). There is some indication of a slight enhancement of near-inertial wind energy flux to the ocean during the 2006 austral summer survey compared to the 2005 austral winter survey north of the SAF (Figs. 11e–h). However, the lack of moored time series data does not allow us to properly assess whether there is a seasonal signal in inertial motions and near-inertial wind energy flux to the ocean that may explain our observation of enhanced diffusivity in summer.

3) SUMMARY OF WIND FORCING

The wind energy supplied to the ocean during both the 2005 austral winter and 2006 austral summer surveys is a potential source of the energy needed to support the observed diffusivity below the mixed layer. Wind forcing may excite near-inertial currents in the upper ocean. We find that the near-inertial wind work is approximately 50% of the net wind work in the 2005 austral winter and 2006 austral summer surveys.

The energy flux required to maintain ϵ is given as $\Pi_\epsilon = \rho_o \int_{1000\text{m}/27.4}^{\text{MLD}} \epsilon\, dz$, where ρ_o is the mean density of the water column and ϵ is integrated between the base of the mixed layer and $\sigma_\theta = 24.7$ kg m^{-3} or 1000 m, whichever is shallowest. Figure 12 shows a comparison of the energy flux required to maintain the observed ϵ and the estimated energy flux from the wind. The net wind energy flux and approximated near-inertial wind energy flux is able to supply some of the necessary

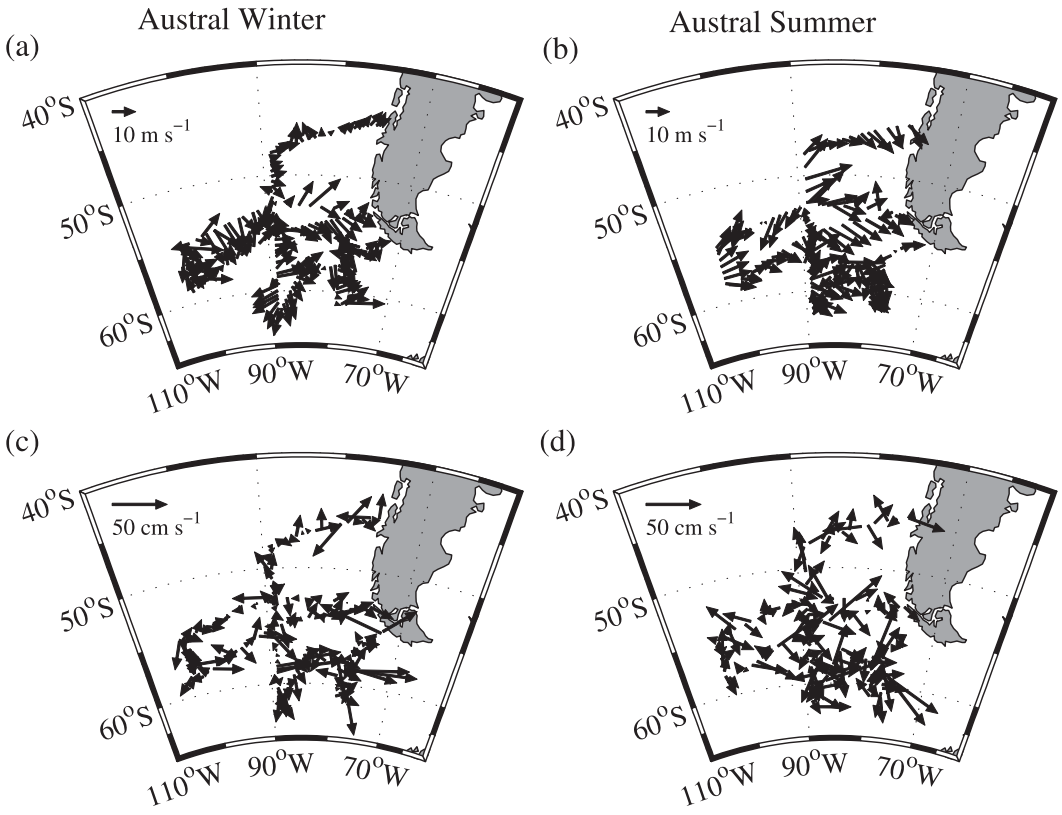

FIG. 9. The 2005 austral winter and 2006 austral summer 5-min mean (a),(b) wind vectors (m s^{-1}) from shipboard IMET data and (c),(d) surface velocity (cm s^{-1}) from SADCP. Wind and surface current vectors are shown every 6 h along the survey track.

energy to sustain the depth-integrated rate of turbulent kinetic dissipation. During the 2005 austral winter and 2006 austral summer surveys, periods of enhanced wind variability appear to provide sufficient energy flux to sustain the rate of turbulent kinetic energy dissipation. We find that most of the wind energy flux can be dissipated in the southeast Pacific; this suggests that only a small percentage of wind energy is free to propagate to the abyssal ocean.

c. *Other potential drivers of the observed* ϵ

Mesoscale eddies and internal wave breaking are other possible processes that may contribute to the enhanced ϵ in the southeast Pacific sector of the Southern Ocean. Ferrari and Polzin (2005) find that both isopycnal mixing by eddies and diapycnal turbulence are required to explain the potential temperature–salinity (T–S) variability in the Mediterranean Water of the eastern North Atlantic. In both surveys, the T–S variability is largest near the SAF and PF and decreases with increasing distance from the frontal region (Fig. 2). The T–S variability in the frontal region during the 2006 austral summer survey is larger than that observed during the 2005 austral winter survey. For both surveys the T–S variability is suggestive of mesoscale eddy stirring that may be arrested by diapycnal turbulence.

Another possible source of the energy required to explain the observed ϵ is the breaking of remotely generated internal waves that propagate into the region. Plueddemann and Farrar (2006) observe an upward energy flux in the pycnocline from a mooring record in the Pacific Ocean at 10°N. They suggest that this was the result of a vertically propagating near-inertial wave. Shcherbina et al. (2003) find upward propagation of internal wave energy between 500 and 2500 m in the Japan Sea. In the Southern Ocean enhanced diffusivities throughout the water column are found near the frontal region over complex topography (Sloyan 2005). It is suggested that the interaction between the mean geostrophic current and bottom topography generates lee waves that locally enhances the water column diffusivity but may also propagate into the ocean interior. Upstream of the survey region the ACC passes through deep fractures in the southeast Pacific Ridge–Eltanin Fracture Zone (140°W). Internal waves generated at the ridge may propagate into the southeast Pacific sector of

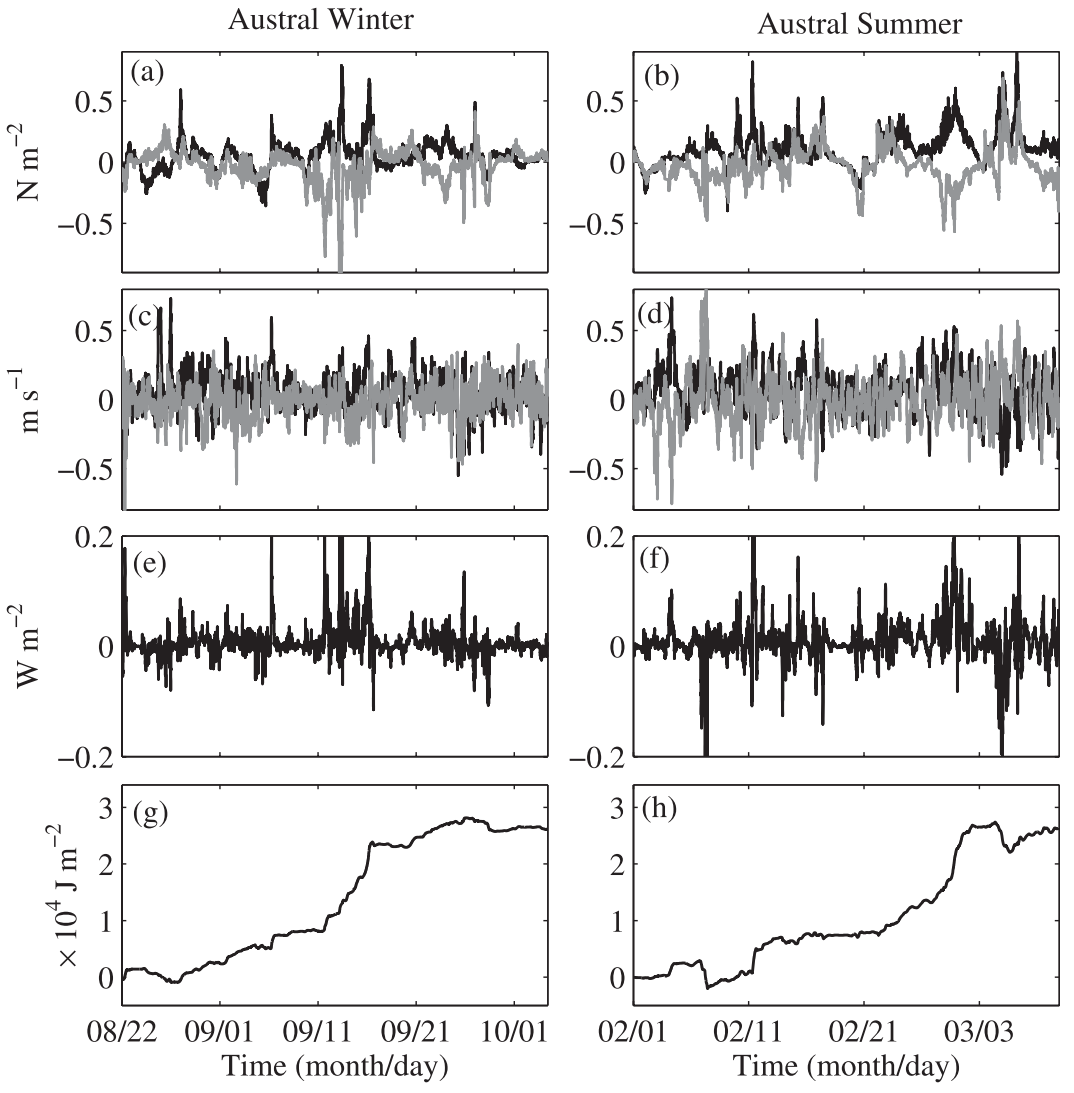

FIG. 10. The 2005 austral winter and 2006 austral summer (a),(b) 5-min mean zonal (black) and meridional (gray) wind stresses (N m^{-2}); (c),(d) 5-min mean zonal (black) and meridional (gray) surface current (m s^{-1}); (e),(f) net wind energy flux (W m^{-2}); and (g),(h) cumulative wind work ($\times 10^4$ J m^{-2}).

the Southern Ocean where dissipation of their energy results in enhanced diffusivity near the base of the mixed layer or in the frontal region.

6. Discussion

Enhanced diffusivity $O(10^{-3}$ to 10^{-4} m^2 s$^{-1})$ is found below the shallow mixed layer (MLD $\leq$ 60 m) north of the SAF in the 2005 austral winter and 2006 austral summer surveys, whereas only background levels of diffusivity are found beneath the deep mixed layer in the SAMW formation region in austral winter. Surrounding the SAF, enhanced diffusivity below the mixed layer to $\sigma_\theta = 27.4$ is found in both surveys. The enhanced diffusivity surrounding the SAF penetrates farther into the water column than diffusivity north of the SAF. All profiles show a decrease in the magnitude of diffusivity and buoyancy flux with increasing depth. Mixing estimates and the vertical decay of diffusivity with depth found in this study are similar to previous studies (Cisewski et al. 2005; Thompson et al. 2007).

Weak salt fingering is only found near the SAF in SAMW density layers during the 2006 austral summer. Wind forcing is similar for both survey periods. Over the survey region, the wind energy flux into the ocean associated with high-frequency wind fluctuations may excite near-inertial motions in the upper ocean, leading to near-inertial internal waves that propagate through the mixed layer to the underlying stratified ocean. This energy flux is dissipated by breaking waves in the ocean

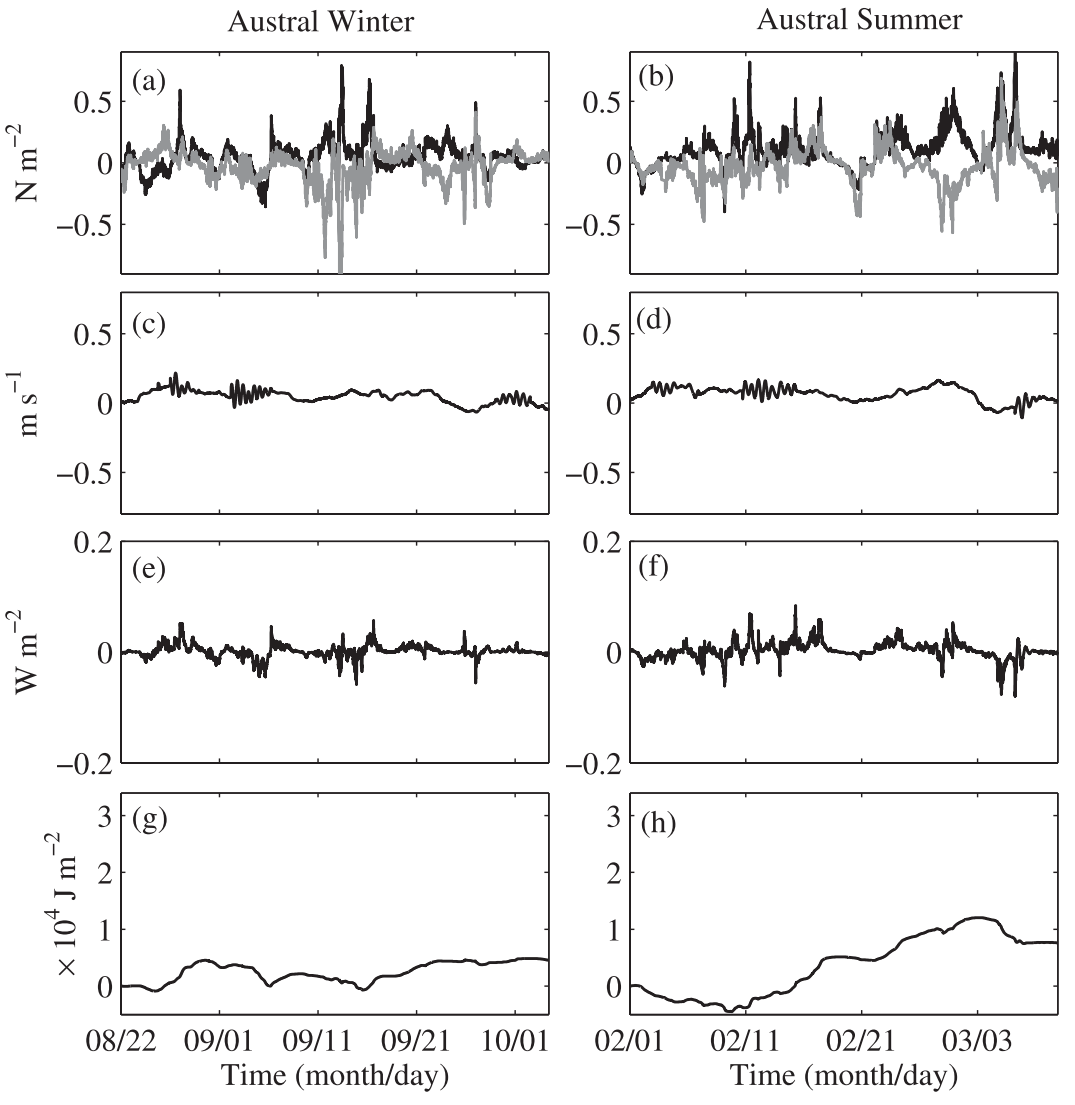

FIG. 11. The 2005 austral winter and 2006 austral summer (a),(b) 5-min mean zonal (black) and meridional (gray) wind stresses (N m^{-2}); (c),(d) 5-min approximated zonal near-inertial surface current (m s^{-1}); (e),(f) near-inertial wind energy flux (W m^{-2}); and (g),(h) near-inertial cumulative wind work ($\times 10^4$ J m^{-2}).

interior. We suggest that some of the energy required to maintain the enhanced diffusivity during the 2005 austral winter and 2006 austral summer surveys may be supplied by high frequency wind forcing at the ocean surface. However, moored time series data are needed to thoroughly assess the relationship between the wind forcing and enhanced diffusivity below the mixed layer and its seasonal variability. Other processes, including mesoscale eddies and propagation of remotely forced internal waves into the region, may also contribute energy to sustain the observed diffusivity. A more comprehensive field program is needed to determine the exact balance amongst the wind energy flux and other sources of energy that sustain the diffusivity in the southeast Pacific sector of the Southern Ocean.

The turbulent kinetic energy dissipation rate strongly influences the interior ocean stratification. Three monthly average stratification profiles between 110° and 90°W, determined from Argo profiles near and 3° equatorward of the SAF, clearly show a decrease in ocean interior stratification (50–400 m) from austral summer (January–March) to austral autumn (April–June) prior to the onset of deep convective mixing in austral winter and early spring (Fig. 13). The buoyancy flux (5) beneath the mixed layer should be comparable to the time rate of change of potential energy of the interior ocean determined from stratification profiles in the SAMW formation region.

Following Arneborg (2002), the change in potential energy between two stratification profiles is

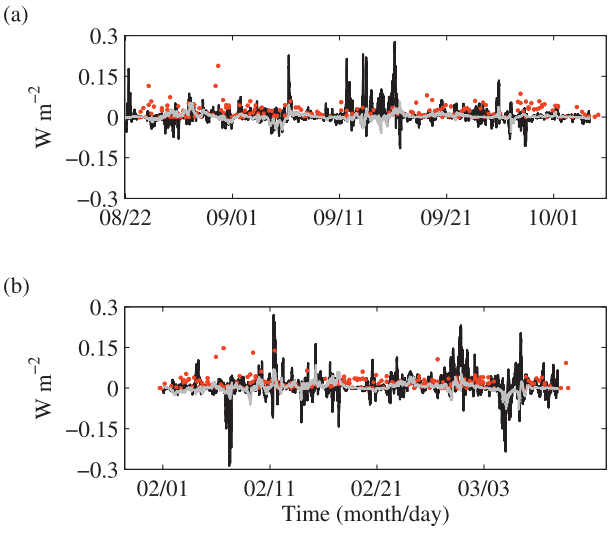

FIG. 12. Comparison of the net wind energy flux (black) and near-inertial wind energy flux (gray) to the ocean and the required energy flux to maintain the depth-integrated ϵ (red diamond) between the base of the mixed layer and $\sigma_\theta = 27.4$ kg m^{-3} or 1000 m for the (a) 2005 austral winter and (b) 2006 austral summer.

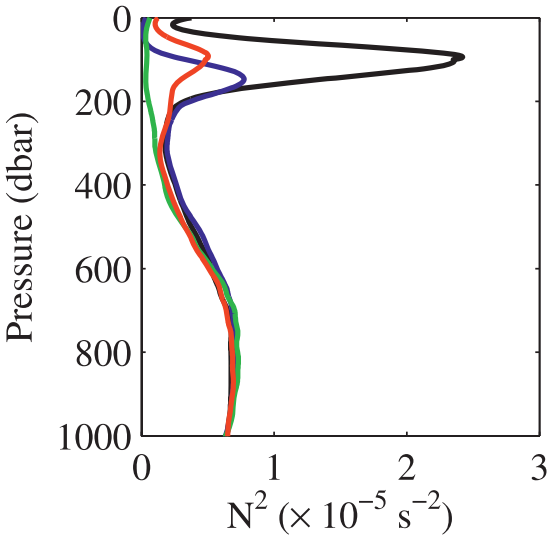

FIG. 13. Mean seasonal stratification N^2 in the southeast Pacific (110°–90°W) from January to March (black), April to June (blue), July to September (green), and October to December (red). Argo profiles used are from January 2003 to May 2007, and only Argo profiles between the SAF and 3° equatorward of the front are used. The position of the SAF is from Orsi et al. (1995).

$$\Delta E = \frac{1}{12}\rho_0(N_A^2 - N_B^2)h^3 a, \tag{7}$$

where N_A^2 and N_B^2 represent the stratification profile at state A and B, h is the water layer thickness of the portion of the N^2 profile considered, ρ_0 is background density, and a is the horizontal area of the mixing region. From (7) the rate of change in potential energy with time is

$$\Delta E_t = \frac{1}{\Delta t}\left[\frac{1}{12}\rho_0(N_A^2 - N_B^2)h^3 a\right]_{t_0}^{t_o+\Delta t}, \tag{8}$$

where t_0 and Δt are the initial time and time step between stratification profiles, respectively. Multiplying (5) by $h\rho a$, we have

$$\Delta E_t = \frac{1}{\Delta t}\left[\frac{1}{12}\rho_0(N_A^2 - N_B^2)h^3 a\right]_{t_0}^{t_o+\Delta t} \cong -h\rho a J_b \cong h\rho a(\Gamma\langle\epsilon\rangle). \tag{9}$$

The observed 2006 austral summer buoyancy flux for SAMW ($26.9 < \sigma_\theta < 27.05$ kg m^{-3}) for the region surrounding the SAF/PF and north of the SAF corresponds to approximately the same area a, background density ρ_0, and water column thickness h used to estimate stratification change between summer and late autumn for the water column between 50 and 400 m (Fig. 13). Therefore, dividing (9) by $h\rho_0 a$ provides an independent comparison of the buoyancy flux required to explain the time rate of change of potential energy, determined from the evolution of the interior stratification of the water column, with an estimate of the buoyancy flux from the observed mixing. The buoyancy flux determined from the evolution of the stratification profile is 0.57×10^{-8} m^2 s^{-3}. This is comparable to the observed buoyancy flux estimated from ϵ, for the 2006 austral summer, of 4.0×10^{-8} m^2 s^{-3}. This suggests that interior ocean turbulent kinetic energy dissipation can provide the necessary energy to explain the evolution of interior ocean stratification between austral summer and autumn.

We suggest that during austral summer and autumn enhanced ϵ, beneath the mixed layer, substantially modifies the interior stratification, resulting in a buoyancy loss that is similar to the buoyancy loss during the winter convective period (Fig. 13). Reduced interior ocean stratification of the water column beneath the mixed layer during austral summer and autumn preconditions the water column for the rapid and efficient development of deep mixed layers in the AAIW and SAMW formation region during austral winter and early spring. This study suggests that interior ocean turbulent kinetic dissipation is an important process preceding the austral winter formation of AAIW and SAMW in the southeast Pacific sector of the Southern Ocean.

7. Conclusions

Two hydrographic surveys in the southeast Pacific sector of the Southern Ocean show enhanced diffusivity $O(10^{-3}$ to 10^{-4} m^2 s$^{-1})$ below the mixed layer north of

the SAF that decays to $O(<10^{-4}\ m^2\ s^{-1})$ by approximately 1000 m. Enhanced diffusivity is also found within the SAF frontal zone. The energy required to maintain the observed diffusivity is likely to be supplied from a number of sources including wind forcing at the ocean surface, mesoscale eddies, and propagation of remotely forced internal waves into the region. A more comprehensive observational program should determine the balance among the wind energy flux and other sources of energy needed to sustain the diffusivity in the southeast Pacific sector of the Southern Ocean.

The observed 2006 austral summer survey buoyancy flux ($4.0 \times 10^{-8}\ m^2\ s^{-3}$) surrounding the SAF is comparable to the mean buoyancy flux ($0.57 \times 10^{-8}\ m^2\ s^{-3}$) associated with the evolution of the interior stratification from austral summer to autumn, determined from Argo floats. The buoyancy flux, resulting from the enhanced diffusivity below the mixed layer, between austral summer and autumn significantly reduces the upper-ocean stratification prior to the onset of winter convective mixing in the AAIW and SAMW formation region. The reduction of the interior ocean stratification during austral summer and autumn preconditions the water column for the rapid development of deep mixed layers and efficient AAIW and SAMW formation during austral winter and early spring.

Acknowledgments. This paper is a contribution to the CSIRO Climate Change Research Program. BMS was funded by CSIRO Wealth from Oceans Flagship and the Australian Climate Change Science Program. We are grateful to the National Science Foundation for support of this work under NSF Grants OCE-0327544 (LDT, TKC, and JH) and OCE-0424774 (RF). We thank the captain and crew of the R/V *Knorr* and the SIO Oceanographic Data Facility for their excellent technical and logistical support during the surveys. Laura Herraiz Borreguero provided quality-controlled Argo data used in this study. Jules Hummon and Eric Firing gave advice and support for the ADCP data collection. Discussions with Trevor McDougall, Kurt Polzin, and Alberto Naviera Garabato and comments from Eric Firing and the reviewers were helpful.

REFERENCES

Alford, M. H., 2001: Internal swell generation: the spatial distribution of energy flux from the wind to mixed layer near-inertial motions. *J. Phys. Oceanogr.,* **31,** 2359–2368.

Arneborg, L., 2002: Mixing efficiencies in patchy turbulence. *J. Phys. Oceanogr.,* **32,** 1496–1506.

Banks, H., and N. L. Bindoff, 2003: Comparison of observed temperature and salinity changes in the Indo-Pacific with results from the coupled climate model HadCM3: Processes and mechanisms. *J. Climate,* **16,** 156–166.

Bindoff, N. L., and T. J. McDougall, 2000: Decadal changes along an Indian Ocean section at 32°S and their interpretation. *J. Phys. Oceanogr.,* **30,** 1207–1222.

Bray, N. A., and N. P. Fofonoff, 1981: Available potential energy for MODE eddies. *J. Phys. Oceanogr.,* **11,** 30–46.

Bryden, H. L., E. L. McDonagh, and B. A. King, 2003: Changes in ocean water mass properties: Oscillations or trends. *Science,* **300,** 2086–2088.

Chereskin, T. K., and C. L. Harris, 1997: Shipboard acoustic Doppler current profiling during the WOCE Indian Ocean expedition: I10. Scripps Institution of Oceanography Reference Series Tech. Rep. 97–14, 137 pp.

Cisewski, B., V. H. Strauss, and H. Prandke, 2005: Upper-ocean vertical mixing in the Antarctic Polar Front zone. *Deep-Sea Res. II,* **52,** 1087–1108.

Crawford, W. R., 1986: A comparison of length scales and decay times of turbulence in stably stratified flows. *J. Phys. Oceanogr.,* **16,** 1847–1854.

D'Asaro, E. A., 1985: Upper ocean temperature structure, inertial currents, and Richardson numbers observed during strong meteorological forcing. *J. Phys. Oceanogr.,* **15,** 943–962.

de Boyer Montégut, C., G. Madec, A. S. Fischer, A. Lazar, and D. Iudicone, 2004: Mixed layer depth over the global ocean: An examination of profile data and a profile-based climatology. *J. Geophys. Res.,* **109,** C12003, doi:10.1029/2004JC002378.

Dillon, T. M., 1982: Vertical overturns: A comparison of Thorpe and Ozmidov length scales. *J. Geophys. Res.,* **87,** 9601–9613.

Dong, S., J. Sprintall, S. T. Gille, and L. Talley, 2008: Southern Ocean mixed-layer depth from Argo float profiles. *J. Geophys. Res.,* **113,** C06013, doi:10.1029/2006JC004051.

Ferrari, R., and K. L. Polzin, 2005: Fine structure of the *T–S* relation in the eastern North Atlantic. *J. Phys. Oceanogr.,* **35,** 1437–1454.

Ferron, B., H. Mercier, K. Speer, A. Gargett, and K. Polzin, 1998: Mixing in the Romanche Fracture Zone. *J. Phys. Oceanogr.,* **28,** 1929–1945.

Galbraith, P. S., and D. E. Kelley, 1996: Identifying overturns in CTD profiles. *J. Atmos. Oceanic Technol.,* **13,** 688–702.

Gille, S. T., 2002: Warming of the Southern Ocean since the 1950s. *Science,* **295,** 1275–1277.

Hanawa, K., and L. D. Talley, 2001: Mode waters. *Ocean Circulation and Climate,* G. Siedler, J. Church, and J. Gould, Eds., Academic Press, 373–386.

Holte, J., and L. Talley, 2009: A new algorithm for finding mixed layer depths with application to Argo data and Subantarctic Mode Water formation. *J. Atmos. Oceanic Technol.,* **26,** 1920–1939.

Jackett, D., T. J. McDougall, R. Feistel, D. G. Wright, and S. M. Griffies, 2006: Algorithms for density, potential temperature, conservative temperature, and the freezing temperature of seawater. *J. Atmos. Oceanic Technol.,* **23,** 1709–1728.

Johnson, H. L., and C. Garrett, 2004: Effects of noise on Thorpe scales and run lengths. *J. Phys. Oceanogr.,* **34,** 2359–2372.

Karsten, R. H., and J. Marshall, 2002: Constructing the residual circulation of the ACC from observations. *J. Phys. Oceanogr.,* **32,** 3315–3327.

Ledwell, J. R., A. J. Watson, and C. S. Law, 1993: Evidence for slow mixing across the pycnocline from an open-ocean tracer-release experiment. *Nature,* **364,** 701–703.

Marsh, R., A. J. G. Nurser, A. P. Megann, and A. L. New, 2000: Water mass transformation in the Southern Ocean of a global isopycnal coordinate GCM. *J. Phys. Oceanogr.,* **30,** 1013–1045.

McCartney, M. S., 1977: Subantarctic Mode Water. *Deep-Sea Res.,* **24,** 103–119.

——, 1982: The subtropical recirculation of mode waters. *J. Mar. Res.,* **40,** 427–464.

McDonagh, E. L., H. L. Bryden, B. A. King, R. J. Saunders, S. A. Cunningham, and R. Marsh, 2005: Decadal changes in the south Indian Ocean thermocline. *J. Climate,* **18,** 1575–1590.

McDougall, T. J., S. Thorpe, and C. Gibson, 1988: Small-scale turbulence and mixing in the ocean: A glossary. *Small-Scale Turbulence and Mixing in the Ocean,* J. C. J. Nihoul and B. M. Jamert, Eds., Elsevier, 3–9.

Orsi, A. H., T. Whitworth III, and W. D. Nowlin Jr., 1995: On the meridional extent and fronts of the Antarctic circumpolar current. *Deep-Sea Res. I,* **42,** 641–673.

Osborn, T. R., 1980: Estimates of the local rate of vertical diffusion from dissipation measurements. *J. Phys. Oceanogr.,* **10,** 83–89.

Plueddemann, A. J., and J. T. Farrar, 2006: Observations and models of the energy flux from the wind to the mixed-layer inertial currents. *Deep-Sea Res. II,* **53,** 5–30.

Ribbe, J., and M. Tomczak, 1997: On convection and formation of Subantarctic Mode Water in the Fine Resolution Antarctic Model (FRAM). *J. Mar. Syst.,* **13,** 137–154.

Rintoul, S. R., and M. H. England, 2002: Ekman transport dominates local air–sea fluxes in driving the variability of Subantarctic Mode Water. *J. Phys. Oceanogr.,* **32,** 1308–1321.

Ruddick, B., 1983: A practical indicator of the stability of the water column to double-diffusive activity. *Deep-Sea Res.,* **30,** 11051107.

Sallée, J.-B., N. Wienders, K. Speer, and R. Morrow, 2006: Formation of Subantarctic Mode Water in the southeast Indian Ocean. *Ocean Dyn.,* **56,** 525–542, doi:10.1007/s10236-005-0054-x.

——, K. Speer, S. R. Rintoul, and S. Wijffels, 2010: Southern Ocean thermocline ventilation. *J. Phys. Oceanogr.,* **40,** 509–529.

Shcherbina, A. Y., L. D. Talley, E. Firing, and P. Hacker, 2003: Near-surface frontal zone trapping and deep upward propagation of internal wave energy in the Japan/East Sea. *J. Phys. Oceanogr.,* **33,** 900–912.

Sloyan, B. M., 2005: Spatial variability of mixing in the Southern Ocean. *Geophys. Res. Lett.,* **32,** L18603, doi:10.1029/2005GL023568.

——, and S. R. Rintoul, 2001: Circulation, renewal, and modification of Antarctic Mode and Intermediate Water. *J. Phys. Oceanogr.,* **31,** 1005–1030.

Smith, S. R., M. A. Bourassa, and R. J. Sharp, 1999: Establishing more truth in true winds. Center for Ocean-Atmospheric Prediction Studies Tech. Rep. 16, 939–952.

St. Laurent, L. C., J. M. Toole, and R. W. Schmitt, 2001: Buoyancy forcing by turbulence above rough topography in the abyssal Brazil Basin. *J. Phys. Oceanogr.,* **31,** 3476–3495.

Talley, L. D., 1999: Some aspects of ocean heat transport by the shallow, intermediate and deep overturning circulations. *Mechanisms of Global Climate Change at Millennial Time Scales, Geophys. Monogr.,* Vol. 112, Amer. Geophys. Union, 1–22.

Thompson, A. F., S. T. Gille, J. A. MacKinnon, and J. Sprintall, 2007: Spatial and temporal patterns of small-scale mixing in Drake Passage. *J. Phys. Oceanogr.,* **37,** 572–592.

Thorpe, S. A., 1977: Turbulence and mixing in a Scottish loch. *Philos. Trans. Roy. Soc. London,* **289A,** 125–181.

——, 2005: *The Turbulent Ocean*. Cambridge University Press, 439 pp.

van Loon, H., and D. J. Shea, 1988: A survey of the atmospheric elements at the ocean's surface south of 40°S. *Antarctic Ocean and Resource Variability,* D. Sahrhage, Ed., Springer-Verlag, 3–20.

Wong, A., N. Bindoff, and J. Church, 1999: Large-scale freshening of intermediate waters in the Pacific and Indian Oceans. *Nature,* **400,** 440–443.

Wunsch, C., 1998: The work done by the wind on the oceanic general circulation. *J. Phys. Oceanogr.,* **28,** 2332–2340.

Yuan, X., 2004: High-wind-speed evaluation in the Southern Ocean. *J. Geophys. Res.,* **109,** D13101, doi:10.1029/2003JD004179.